

Harmonic generation of graphene quantum dots in Hartree-Fock approximation

Kainan Chang,^{*,†} Ying Song,[‡] Yuwei Shan,[†] and Jin Luo Cheng^{*,†}

[†]*GPL Photonics Laboratory, State Key Laboratory of Luminescence Science and Technology, Changchun Institute of Optics, Fine Mechanics and Physics, Chinese Academy of Sciences, Changchun 130033, China.*

[‡]*State Key Laboratory of Advanced Manufacturing for Optical Systems, Changchun Institute of Optics, Fine Mechanics and Physics, Chinese Academy of Sciences, Changchun 130033, China.*

E-mail: knchang@ciomp.ac.cn; jlcheng@ciomp.ac.cn

Abstract

We theoretically investigate harmonic generation in graphene quantum dots under linearly polarized optical pulses, focusing on excitonic effects. Combining the tight-binding model and the single-particle density matrix approach, we derive semiconductor Bloch equations under a static-screened Hartree-Fock approximation. This framework characterizes the electron-electron interaction through local Hartree potentials for direct Coulomb interaction and nonlocal Fock potentials for exchange interaction. Distinct configurations of Hartree and Fock terms yield various approximation methods, including the independent-particle approximation, the mean-field approximation, the random phase approximation, and the excitonic effects. We thoroughly analyze how these approximation methods affect the electronic energy levels, linear optical absorption, and nonlinear harmonic generation. Within excitonic effects, we present the dependence

of harmonic generation on the geometric variations of graphene quantum dots (sizes, triangular/hexagonal shapes, and armchair/zigzag edges) and the amplitude and polarization of electric fields. Our findings show that excitonic effects significantly enhance optical responses of graphene nanostructures. For a dot ensemble formed by randomly oriented graphene quantum dots, only odd-order harmonics exist along the polarization direction of the incident light. Crucially, harmonic generation in graphene quantum dots exhibits high tunability via geometric configuration, making them promising candidates for nonlinear optical nanodevices.

Graphene, as the first fabricated two-dimensional material, has attracted enormous attention due to its chemical stability, mechanical robustness, high carrier mobility,^{1,2} ultrafast carrier dynamics,^{3,4} wideband absorption from THz to visible,^{1,5-7} and extremely strong optical nonlinearity.^{8,9} These properties arise from its linear dispersion and can be well controlled by Fermi levels through electric gating or chemical doping techniques.¹⁰⁻¹² Given the easy integration with photonic structures, graphene is ideal for realizing photonic devices with novel functionalities.

However, applications in nano-electronic and nano-photonic devices are also limited by the zero bandgap,^{13,14} which can be conquered by the advancements in nano-fabrication techniques¹⁵⁻¹⁸ via engineering the size, shape, or edge of graphene on the nanoscale to form various graphene nanostructures, including nanoribbons,¹⁹⁻²¹ flakes^{22,23} and quantum dots.^{24,25} In particular, graphene quantum dots (GQDs) are zero-dimensional fragments of graphene with a size smaller than 100 nm, and have been widely applied in photovoltaics, light-emitting diodes, batteries, fuel cells, memory devices, sensitizers in solar cells, bioimaging, etc.^{22,24,26-28}

Recent studies have focused on understanding the nonlinear optical properties of GQDs. Cox *et al.* found that the second- and third-order polarizabilities of GQD exceed those of noble metal nanoparticles with similar lateral size,²⁹ and the physical mechanism is attributed to the strong plasmonic near-field enhancement; its polarization can be precisely tuned and

controlled by applying an external electric field.³⁰ Aguillon *et al.*²³ theoretically investigated the effect of vacancy defects on the second harmonic generation (SHG) of GQD, and obtained an efficient SHG even for vacancy concentrations as low as one per several thousands of lattice atoms. Avchyan *et al.*³¹ and Gnawali *et al.*^{32,33} showed the dependence of harmonic generation on the size, edge, and shape of GQD. Among these works, the Coulomb interaction is considered either at the level of mean-field approximation (MFA) or random-phase approximation (RPA), while excitonic effects (EXE) are not taken into account. However, it is well known that EXE in two-dimensional materials with a bandgap are extremely important for both linear^{18,34} and nonlinear^{35,36} optical properties due to the insufficient screening of the Coulomb interaction, and it is of fundamental importance to understand how it affects nonlinear optical responses in GQDs.

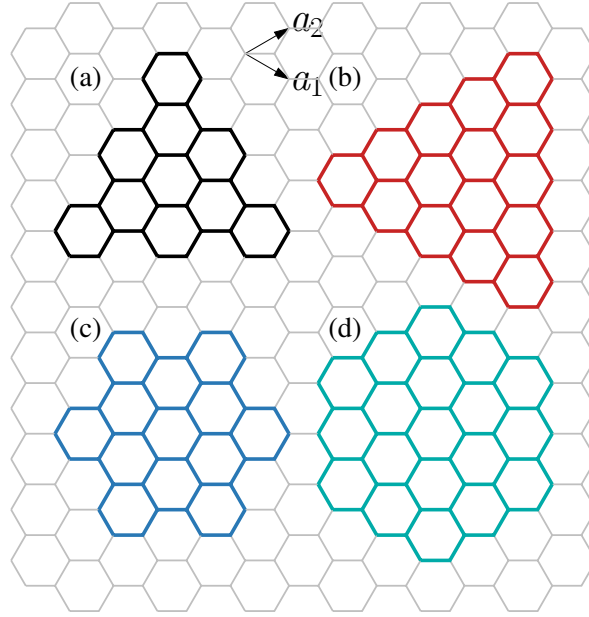


Figure 1: Illustration of GQDs with different edges and shapes: (a) 3-AC-TQD (b) 5-ZZ-TQD, (c) 2-AC-HQD, and (d) 3-ZZ-HQD. \mathbf{a}_1 and \mathbf{a}_2 indicate the primitive lattice vectors of graphene.

For this purpose, we focus on the harmonic generation in GQDs, with different shapes and edges as shown in Fig. 1. The electronic states of GQDs are calculated in the framework

of tight-binding approximation with the nearest-neighbor coupling, and Coulomb electron-electron interactions at the level of static-screened Hartree-Fock (HF) approximation. The dynamics of applying a strong laser field is described by semiconductor Bloch equations, and their numerical solutions are used to extract the nonlinear susceptibilities. Within our model, the Hartree term of the Coulomb interaction contributes to the local field and RPA, while the Fock term gives rise to EXE. Our results reveal that the EXE has a profound impact on the resonance energy and intensity of the optical responses of GQDs. Furthermore, we also discuss the effects of the size, edge, and shape of GQDs, as well as the amplitude and polarization of the electric field.

Results and discussion

We consider the GQDs, which are nanoflakes with different edges and shapes cut from a monolayer graphene, including equilateral triangular QDs with armchair edges (AC-TQD) or zigzag edges (ZZ-TQD) and hexagonal QDs with armchair edges (AC-HQD) or zigzag edges (ZZ-HQD), as shown in Figs. 1 (a-d), respectively. These GQDs are described by the number of hexagons at each edge as N -AC-TQD, N -ZZ-TQD, N -AC-HQD, and N -ZZ-HQD.

Electronic structures at screened HF approximation

We first discuss how the static-screened HF approximation affects the energy levels of GQD, mainly focusing on the eigenenergies $\varepsilon_{s\sigma}$ from Eq. (14b). From our calculations, the ground states of all studied GQDs can be taken as antiferromagnetic states, which have lower energies. Figures 2 (a), (b), (d), and (e) show energy levels of 4-AC-TQD, 6-ZZ-TQD, 3-AC-HQD, and 4-ZZ-HQD in independent-particle approximation (IPA) and MFA, respectively. Because only the nearest neighbor coupling is considered in the tight-binding model, the electron-hole symmetry is preserved for all considered GQDs in IPA, like that for graphene. Due to the high symmetry of these GQDs, there exist many degeneracies in IPA electronic

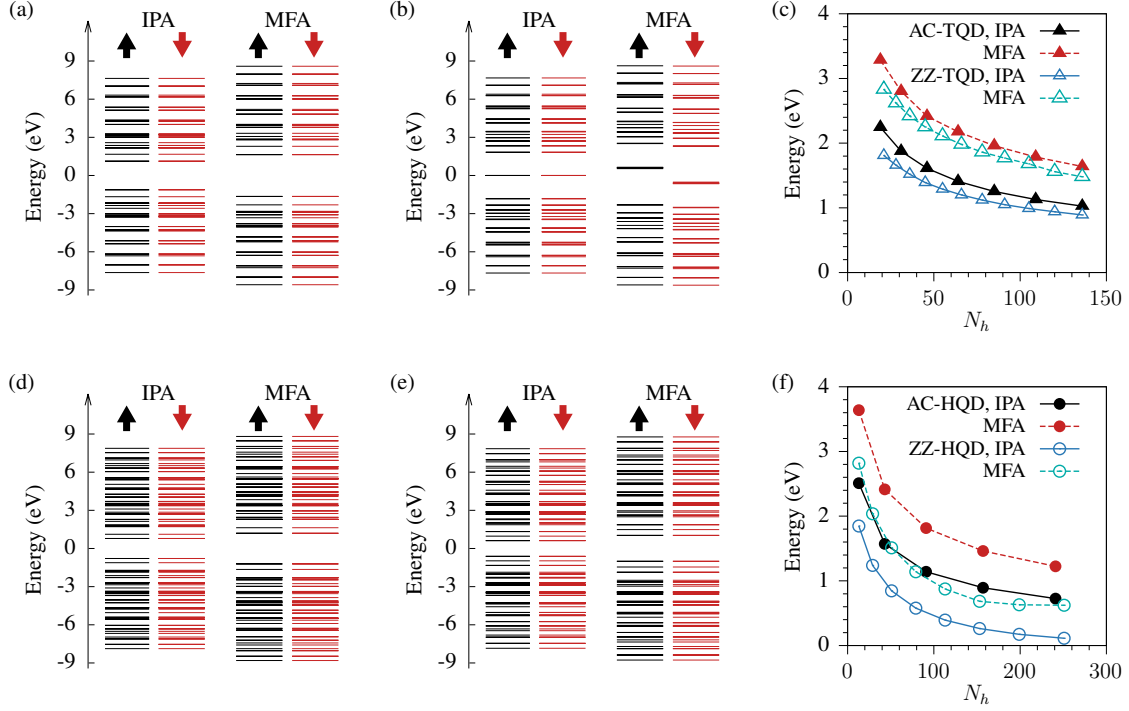


Figure 2: Electronic energy levels at IPA (left panel) and MFA (right panel), for (a) 4-AC-TQD, (b) 6-ZZ-TQD, (d) 3-AC-HQD, (e) 4-ZZ-HQD. Colored arrows mean different spins. Size-dependent bandgap for (c) TQD and (f) HQD.

states, as reported by Güçlü *et al.*¹⁸ Except for the 6-ZZ-TQD, there exists an energy gap between the lowest unoccupied molecular orbital (LUMO) and the highest occupied molecular orbital (HOMO) states; while for 6-ZZ-TQD, there exist 10 degenerate states with zero energy (with the inclusion of spin degeneracy) but only half of them are occupied, which leads to zero gaps. By taking into account the screened HF approximation in MFA, the electronic states for all GQDs are significantly changed. For ZZ-TQD, antiferromagnetic ground state is more stable, and the degeneracy between spin states is broken; however, each spin up state with energy ϵ is accompanied by a spin down state with energy $-\epsilon$. At the same time, all zero-energy states are split into two spin groups with different energies, and each group includes five energy levels with very close energies, which gives a nonzero gap. For other types of GQDs, the total energies for antiferromagnetic ground state and paramagnetic ground state are very close to each other, but the former is slightly lower;

the spin degeneracy and electron-hole symmetry are both preserved, but the energy gaps are widened, which is as expected because the screened HF approximation gives the lowest order of GW correction. Figures 2 (c) and (f) give the dependence of the bandgap on the QD size. In general, the gaps in MFA are larger than those in IPA, indicating the important effects of Coulomb interaction. All gaps decrease with increasing size of GQDs, because of weaker quantum confinement.

Linear optical response

We consider the optical response of the polarization to an applied electric field pulse with a Gaussian envelope function,

$$\mathbf{E}(t) = E_0 \hat{\mathbf{e}}_\Omega e^{-t^2/\Delta_c^2} e^{-i\Omega t} + \text{c.c.}, \quad (1)$$

with the duration Δ_c , the center frequency Ω , and the polarization $\hat{\mathbf{e}}_\Omega$. In the frequency domain, this corresponds to a function with Gaussian peaks as

$$\begin{aligned} \mathbf{E}(\omega) &= \int dt \mathbf{E}(t) e^{i\omega t} \\ &= \sqrt{\pi} \Delta_c \left[\hat{\mathbf{e}}_\Omega e^{-(\omega-\Omega)^2 \Delta_c^2/4} + \hat{\mathbf{e}}_\Omega^* e^{-(\omega+\Omega)^2 \Delta_c^2/4} \right]. \end{aligned} \quad (2)$$

The polarization $\mathbf{P}(t)$ is also a pulse, and its spectra $\mathbf{P}(\omega) = \int dt \mathbf{P}(t) e^{i\omega t}$ are located around the harmonic frequencies $j\Omega$ for integer j . A linear susceptibility tensor is extracted from

$$\chi^{(1);da}(\omega) = \frac{P^d(\omega)}{E^a(\omega)}. \quad (3)$$

In the following calculations, we take $T = 300$ K, $\mu = 0$ eV, and $\Gamma = 20$ fs. For the linear optical process, a simple numerical method to extract the susceptibility spectra is to perform the excitation by a very short laser pulse with the parameters $\Delta_c = 1$ fs, $\hbar\Omega = 3$ eV, and $E_0 = 10^4$ V/m. For all considered geometries, the symmetries determine the

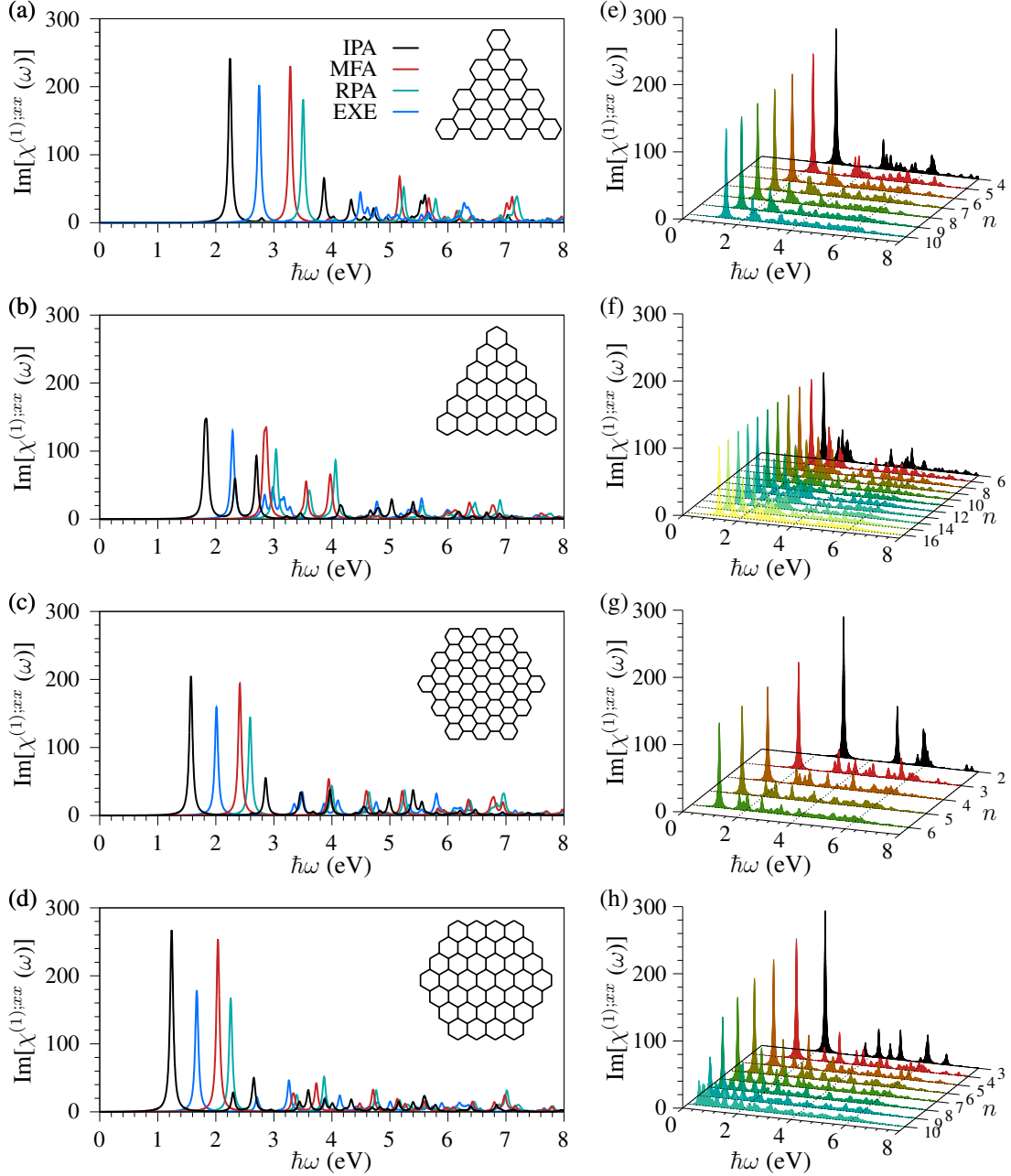


Figure 3: Spectra of $\text{Im}[\chi^{(1);xx}(\omega)]$ for (a) 4-AC-TQD, (b) 6-ZZ-TQD, (c) 3-AC-HQD, (d) 4-ZZ-HQD under different approximations of IPA, MFA, RPA, and EXE. (e-h) QD size dependence of the spectra in EXE for the shapes as those in (a-d).

nonzero susceptibility components as $\chi^{(1);xx} = \chi^{(1);yy}$. The calculated absorption spectra, given by $\text{Im}[\chi^{(1);xx}(\omega)]$, are plotted in Figs.3(a-d) for the GQDs in Figs.2(a, b, d, e), under different approximations of IPA, MFA, RPA, and EXE. Compared with the spectra in IPA, the peaks of those in MFA move to higher energies. It is because that under the

single-particle approximation, the optical absorption processes are directly determined by the energy levels shown in Fig. 2, and the lowest-energy peaks are dictated by the energy gaps.^{37–39} When the Coulomb interaction is taken into account through the Hartree term in RPA, the absorption spectra blue-shift with weaker amplitudes, compared with the case in MFA. The primary reason is that the total electric field experienced by the electrons in RPA is not only the external field $\mathbf{E}(t)$, but also the field induced by the inhomogeneous charge density generated under the optical excitation. Due to the geometric effect, these local plasmons can be excited by plane waves. In this way, the absorption peak locations in RPA are shifted to higher energies corresponding to the local plasmon resonance. When both Hartree and Fock terms are considered in EXE, the absorption spectra red-shift to lower the optical gap, which indicates the formation of excitonic levels. It is also clear that the amplitudes of the first peaks in EXE, associated with the lowest exciton energy, are higher than those in RPA, indicating the enhancement of linear absorption by excitonic effects.

Figures 3 (e–h) show the spectra of $\text{Im}[\chi^{(1);xx}(\omega)]$ for GQDs with different sizes at the level of EXE. The first peaks give a strong absorption at the lowest exciton energy. As the QD size increases, these first peaks move to lower energies, because of the weaker quantum confinement energy for GQDs with larger size; and the amplitudes of spectra become lower, due to the weaker optical transitions.

Nonlinear Optical Response

Then we turn to the nonlinear optical responses, in which the electronic polarization $\mathbf{P}(\omega)$ is located around the center frequencies $j\Omega$ for $j > 1$. Perturbatively, this polarization can be written as⁴⁰

$$\int P^d(j\Omega + \delta) d\delta = \int \frac{d\delta_1 d\delta_2 \cdots d\delta_j}{(2\pi)^j} \sum_{a_1, a_2, \dots, a_j} \chi^{(j); da_1 a_2 \cdots a_j}(\Omega + \delta_1, \Omega + \delta_2, \dots, \Omega + \delta_j) E^{a_1}(\Omega + \delta_1) \cdots E^{a_j}(\Omega + \delta_j). \quad (4)$$

Taking the approximation

$$\sum_{a_1, a_2, \dots, a_j} \chi^{(j)}(\Omega + \delta_1, \Omega + \delta_2, \dots) [\hat{\mathbf{e}}_\Omega]^{a_1} [\hat{\mathbf{e}}_\Omega]^{a_2} \dots \approx \bar{\chi}^{(j);d}(\Omega, \hat{\mathbf{e}}_\Omega), \quad (5)$$

the effective susceptibility $\bar{\chi}^{(j);d}(\Omega, \hat{\mathbf{e}}_\Omega)$ can be calculated through

$$\bar{\chi}^{(j);d}(\Omega, \hat{\mathbf{e}}_\Omega) = \frac{1}{E_0^j} \int_{-\Omega/2}^{\Omega/2} P^d(j\Omega + \delta) d\delta, \quad \text{for } (j \geq 2). \quad (6)$$

Additionally, in the following calculations of nonlinear responses, the pulse duration is fixed at $\Delta_c = 30$ fs.

Spectra of $\mathbf{P}(\omega)$ for $\hbar\Omega = 0.91$ eV and $E_0 = 10^8$ V/m

We first consider the field polarization dependence of the spectra $\mathbf{P}(\omega)$ for different types of GQDs in the EXE approximation, and the results are shown in Fig. 4, where the light parameters are $\hbar\Omega = 0.91$ eV and $E_0 = 10^8$ V/m. It can be seen that all HQDs and TQDs can generate odd-order harmonics up to the thirteenth order, while only TQDs can generate even-order harmonics. For odd-order harmonics, which can be generated from all these four types of GQDs, their polarization is along the field polarization, either along the x or y direction with the response coefficients satisfying $\chi^{(2j+1);x}(\Omega, \hat{\mathbf{x}}) = \chi^{(2j+1);y}(\Omega, \hat{\mathbf{y}})$ and $\chi^{(2j+1);x}(\Omega, \hat{\mathbf{y}}) = \chi^{(2j+1);y}(\Omega, \hat{\mathbf{x}}) = 0$. However, for even-order harmonics, which can only be generated in TQDs, their polarization is always along the y direction with the response coefficients satisfying $\chi^{(2j);y}(\Omega, \hat{\mathbf{x}}) = \chi^{(2j);y}(\Omega, \hat{\mathbf{y}})$ and $\chi^{(2j);x}(\Omega, \hat{\mathbf{x}}) = \chi^{(2j);x}(\Omega, \hat{\mathbf{y}}) = 0$. All these results are consistent with the symmetry analysis. The TQDs have the D_{3h} symmetry, which has no inversion center, and thus the even-order harmonics can be generated, and the perturbative second susceptibility components⁴¹ satisfy $\chi^{(2);yyy} = -\chi^{(2);yxx}$, and the perturbative third-order susceptibility components satisfy $\chi^{(3);xxx} = \chi^{(3);yyy}$. Note that the above discussions are also applicable to the results in other approximations (IPA, MFA, and RPA). Next, we focus on the amplitude of the susceptibility $\chi^{(j);y}(\Omega, \hat{\mathbf{y}})$ for different GQDs.

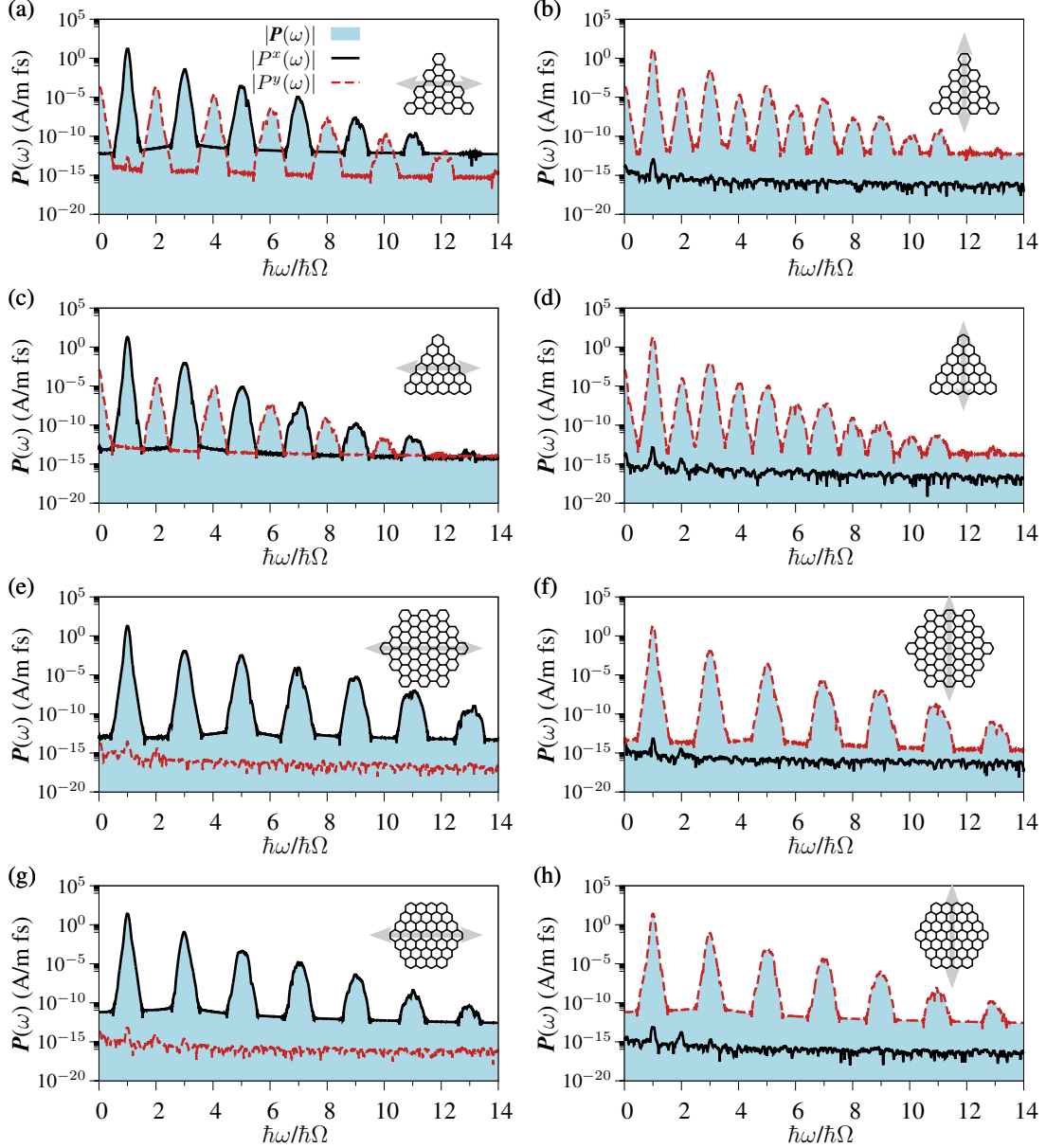


Figure 4: Spectra of $|P(\omega)|$, $|P^x(\omega)|$, and $|P^y(\omega)|$ for different types of GQDs (a, b) 4-AC-TQD, (c, d) 6-ZZ-TQD, (e, f) 3-AC-HQD, and (g, h) 4-ZZ-HQD. The light parameters are $\hbar\Omega = 0.91$ eV, $E_0 = 10^8$ V/m, and the field direction is along the x -direction (a, c, e, g) or the y -direction (b, d, f, h), as shown in the insets.

Susceptibility spectra at different approximations

Now we investigate the effects of Coulomb interaction on the nonlinear optical responses of GQDs. Figure 5 shows the spectra of $\bar{\chi}^{(j);y}(\Omega, \hat{y})$ for SHG, THG, fourth harmonic generation (FOHG), and fifth harmonic generation (FIHG) of a 4-AC-TQD under approximations of

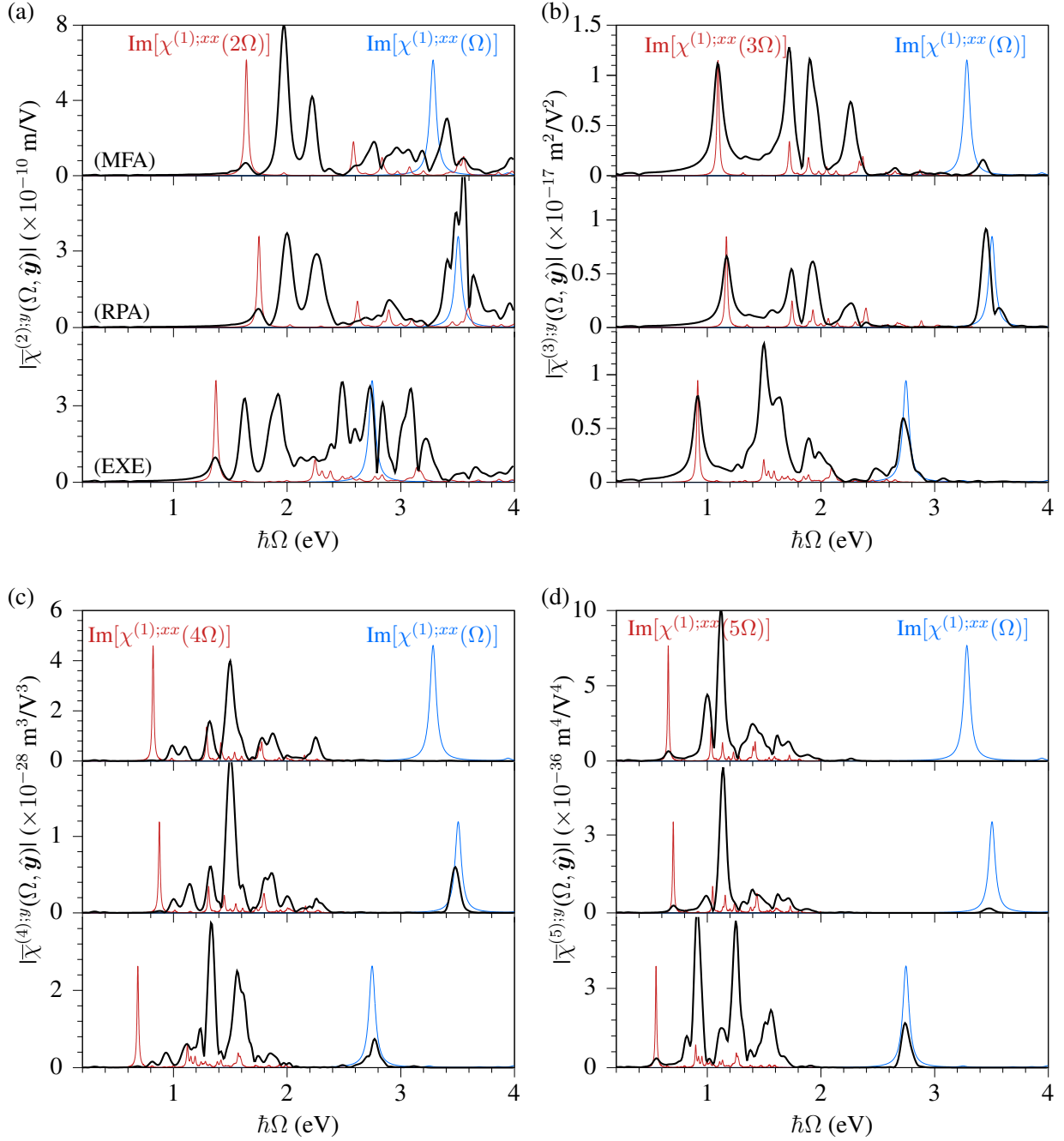


Figure 5: Photon energy $\hbar\Omega$ dependence of $\bar{\chi}^{(n);y}(\Omega, \hat{\mathbf{y}})$ for (a) SHG, (b) THG, (c) FOHG, and (d) FIHG of 4-AC-TQD under the approximations of MFA, RPA, and EXE. The absorption spectra, $\text{Im}[\chi^{(1);xx}(\Omega)]$ (blue lines) and $\text{Im}[\chi^{(1);xx}(j\Omega)]$ (red lines) with $j = 2, 3, 4$, or 5 , are plotted for each approximation.

MFA, RPA, and EXE for a field amplitude of 10^8 V/m. Each figure also shows the linear absorption spectra $\text{Im}[\chi^{(1);xx}(\Omega)]$ to identify the photon energies for one-photon transition

processes as well as $\text{Im}[\chi^{(1);xx}(j\Omega)]$ to identify the photon energies for j -photon transition processes. All spectra show discrete peaks, which are consistent with transitions between discrete energy levels. In the case of MFA, the first peaks of spectra for n th-order harmonic are located at the same energy as the first peaks of $\text{Im}[\chi^{(1);xx}(j\omega)]$, which refers to the n -photon transition processes between the LUMO and HOMO states. With the increase of photon energy, the optical transitions involve high energy states, and more peaks induced by multi-photon optical transitions appear because of the denser energy levels at higher energies, as shown in Fig. 2. In our calculations, the relaxation energy is set to approximately 33 meV, and thus those peaks with similar transition energies merge into a broad peak. When the photon energy reaches $\hbar\Omega \sim 3.28$ eV, which is the energy for the first absorption peak, there should appear the first resonant peak for harmonic generation induced by the one-photon transition process;⁴² however, in GQDs this peak is too small to be visible in the diagram, and the neighboring peaks are induced by the multi-photon resonant peaks. For the cases of RPA and EXE, the energy shift of all spectra is very similar to that of linear absorption, which shows the local plasmonic effects arising from the Hartree term and the EXE arising from the Fock term. Around the first absorption peak, which corresponds to $\hbar\Omega \sim 3.5$ eV in RPA and $\hbar\Omega \sim 2.7$ eV in EXE, the peak values of all harmonic spectra are notably small in MFA, but become well-pronounced in both RPA and EXE. It is primarily attributed to the presence of local plasmonic effects around this energy range in the latter two, resulting in a significant enhancement of the effective electric field experienced by the electrons. These observations highlight the importance of considering many-body interactions and exciton effects in accurately describing the harmonic processes in GQDs.

QD size dependence of the susceptibility spectra

Now we turn to the quantum dot size dependence of the nonlinear susceptibilities $\bar{\chi}^{(j);y}(\Omega, \hat{\mathbf{y}})$ of N -AC-TQD for N from 4 to 9 in EXE under the field $E_0 = 10^8$ V/m, which are shown in Fig. 6. It can be seen that these spectra show similar shapes with all characteristic

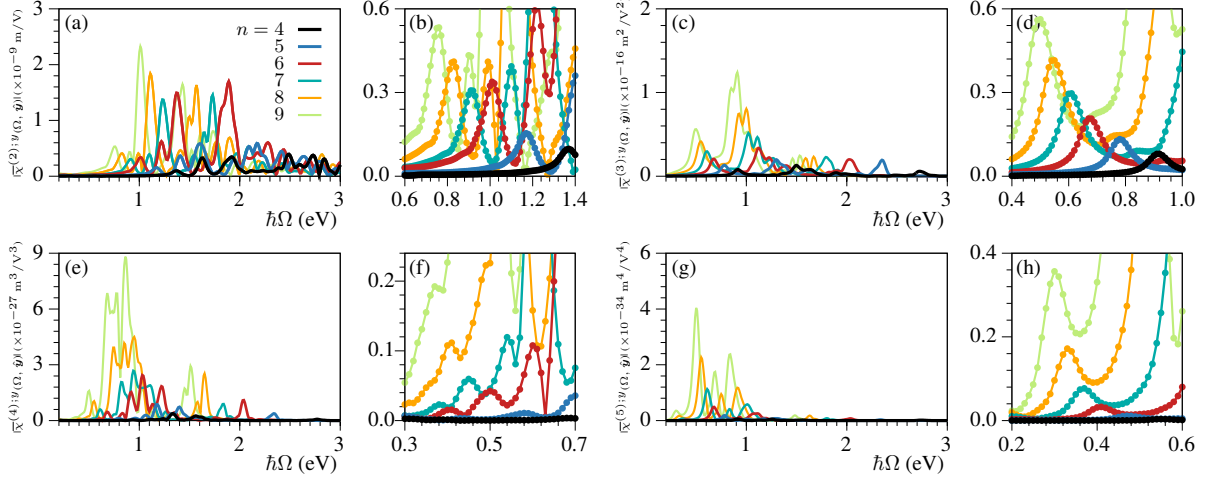


Figure 6: Spectra of nonlinear susceptibilities $|\bar{\chi}^{(j);y}(\Omega, \hat{\mathbf{y}})|$ of N -AC-TQD for different dot size under $E_0 = 10^8$ V/m with (a,b) $j = 2$, (c,d) $j = 3$, (e,f) $j = 4$, and (g,h) $j = 5$. For each harmonic order, the spectra around the first peak corresponding to the j -photon resonant transition are zoomed-in in the right figure.

peaks when the quantum dot size changes, however, both the locations and peak values vary with size. With increasing the QD size, the peak locations red-shift, similar to the absorption spectra in Fig. 3. The reason is that the energy levels become denser, and thus the energy differences between energy levels decrease. The peak values show a complicated dependence on the quantum dot size. For example, in Fig. 6(a), the peak value of the first peak, corresponding to the two-photon resonant transition from the ground state to the lowest exciton state, approximately increases with N , except that the value at $N = 6$ exceeds those at $N = 5$ and $N = 7$, see details in the zoomed-in Fig. 6(b). For other peaks, their peak values also increase with N . Figures 6(c–h) give the spectra of $\bar{\chi}^{(j);y}(\Omega, \hat{\mathbf{y}})$ for $j = 3, 4, 5$ with different quantum dots. These spectra are similar to Figs. 6(a) and (b). For these three spectra, the peak values increase with the increase of quantum dot size. For GQDs with other shapes, all size-dependent properties are similar, except the first peak values of $\bar{\chi}^{(2);y}(\Omega, \hat{\mathbf{y}})$ reach a maximum at $N = 6$, as shown in Fig. S1 in Supporting Information. In general, except for some special sizes, for large quantum dots, the peak locations are red-shifted to lower photon energies, while the peak values increase.

For comparison, we note that the third-order nonlinear susceptibility $\chi^{(3)}$ of the monolayer

graphene, measured via third harmonic generation, ranges from 10^{-19} to 10^{-16} m^2/V^2 in experimental studies^{43,44} and theoretical calculations.^{29,37} In this work, we find that 6-ZZ-HQD shows a maximum value of $\chi^{(3)}$ of 4.7×10^{-16} m^2/V^2 at $\hbar\Omega = 0.9$ eV, representing comparable or superior nonlinear performance relative to monolayer graphene systems. This enhancement in nonlinear response is attributed to the strong quantum confinements and edge effects at the nanoscale.

Field intensity dependence

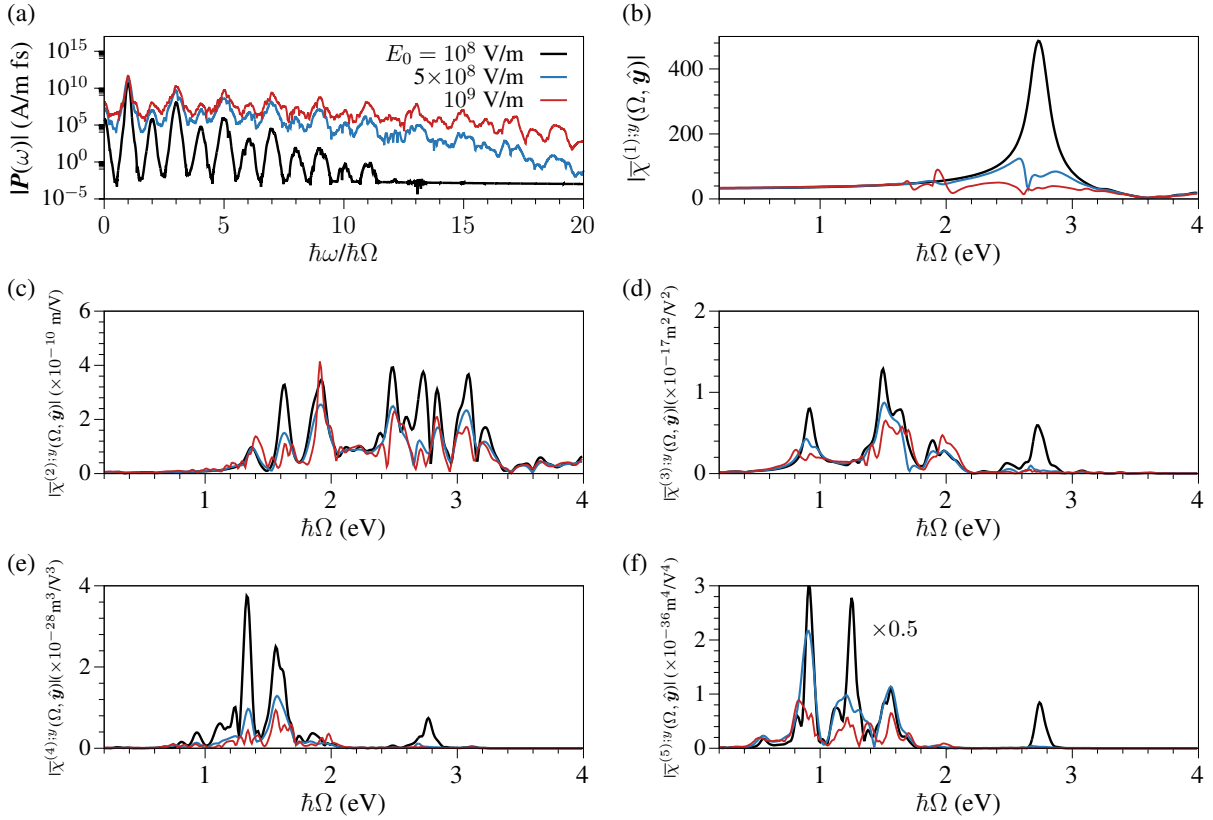


Figure 7: (a) Spectra of $|P(\omega)|$ with $\hbar\Omega = 0.91$ eV and (b-f) spectra of $|\bar{\chi}^{(j);y}(\Omega, \hat{y})|$ of the linear, SHG, THG, FOHG, and FIHG for 4-AC-TQD at different electric fields of $E_0 = 10^8$, 5×10^8 , and 10^9 V/m. Note the values of $|\bar{\chi}^{(5);y}(\Omega, \hat{y})|$ with $E_0 = 10^8$ V/m, represented by the black line in (f), have been multiplied by 0.5.

Figure 7(a) shows the spectra of $|P(\omega)|$ of 4-AC-TQD for $\hbar\Omega = 0.91$ eV under different electric fields, $E_0 = 10^8$, 5×10^8 , and 10^9 V/m. A stronger field strength leads to stronger polarization and higher order harmonics. Figures 7(b-f) give the $|\bar{\chi}^{(j);y}(\Omega, \hat{y})|$ for the linear,

SHG, THG, FOHG, and FIHG under different electric fields. For electric fields of $E_0 = 10^8$ and 5×10^8 V/m, the two spectra show minor changes in the peak locations, but significant reductions in peak amplitudes. This indicates that for these fields, harmonic responses can still be understood as optical transitions between exciton energy levels with saturable absorption effects. In this case, the perturbation theory is applicable. However, for stronger electric fields of $E_0 = 10^9$ V/m, the spectra of $|\bar{\chi}^{(j);y}|$ are dramatically changed in both the peak energies and shapes, indicating a nonperturbative behavior. Note that higher order harmonics are more sensitive to the electric field strength.

Polarization pattern dependence

We now discuss the polarization pattern dependence of harmonic generation for a GQD rotated about the z -direction by an azimuthal angle θ , with incident light polarized along the x -direction. For very weak incident light, the polarization pattern of SHG and THG can be analyzed by considering the symmetry of each type of GQDs. For trigonal GQDs, as previously discussed, they have nonzero SHG susceptibilities due to the D_{3h} symmetry. For unrotated GQD with $\theta = 0$, the nonzero susceptibility components for SHG are $\chi^{(2);xxy} = \chi^{(2);xyx} = \chi^{(2);yxx} = -\chi^{(2);yyy} = \chi^{(2)}$. Thus for a rotated GQD by angle θ , the SHG polarization becomes

$$\mathbf{P}^{(2)}(\theta) = \chi^{(2)} E_x^2 (\hat{x} \sin 3\theta - \hat{y} \cos 3\theta). \quad (7)$$

In contrast, for hexagonal GQDs, SHG vanishes. For all GQD structures discussed in this work, the nonzero susceptibility components for THG are the same, and they are $\chi^{(3);xxxx} = \chi^{(3);yyyy} = \chi^{(3)}$ and $\chi^{(3);xxyy} = \chi^{(3);yyxx} = \chi^{(3);xyxy} = \chi^{(3);yxyx} = \chi^{(3);yyxx} = \chi^{(3);yxyx} = \chi^{(3);yxyx} = \chi^{(3)}/3$. The resulting third harmonic polarization for a rotated GQD is always along the x -direction

as

$$\mathbf{P}^{(3)}(\theta) = \chi^{(3)} E_x^3 \hat{\mathbf{x}}. \quad (8)$$

This reveals a fundamental symmetry distinction – SHG exhibits a threefold (120°) rotational periodicity, while THG remains isotropic and polarized along the same polarization direction as the incident light. All these results are confirmed by our numerical calculations for the incident electric field amplitude of $E_0 = 10^8$ V/m. Furthermore, higher even-order (odd-order) harmonics follow the angular dependence analogous to SHG (THG). However, for stronger electric fields, the polarization pattern dependence deviates from the perturbative expressions in Eqs. (7) and (8). As shown in Fig. 8, which illustrates the θ -dependent susceptibilities for $E_0 = 10^9$ V/m and $\hbar\Omega = 0.91$ eV, the SHG and FOHG spectra retain the threefold rotational periodicity. Unlike the perturbative case, however, the amplitudes of $\bar{\chi}^{(j);x}$ and $\bar{\chi}^{(j);y}$ are no longer equal. Additionally, while THG and FIHG retain predominantly x -direction polarization, they exhibit a near sixfold rotational periodicity.

Many experiments are performed on GQD ensembles formed by randomly orientated GQDs, and the measured polarization is proportional to $\frac{1}{2\pi} \int_0^{2\pi} \mathbf{P}^{(j)}(\theta) d\theta$. For very weak incident light, utilizing Eqs. (7) and (8), the SHG for GQD ensembles vanishes, while the THG remains unchanged. In fact, this can also be understood through the symmetry consideration. A GQD ensemble has isotropic symmetry for which all even-order responses vanish due to the inversion symmetry, while all odd-order responses have the polarization direction aligned with the external field. For the nonperturbative case, the polarization of a GQD ensemble is obtained by numerically integrating $\mathbf{P}^{(j)}(\theta)$ over θ , yielding results similar to the perturbative case. Consequently, for the macroscopic response in GQD ensembles, only odd-order harmonics produce nonvanishing isotropic polarization along the same direction as the incident light, consistent with results for in-plane isotropic systems.

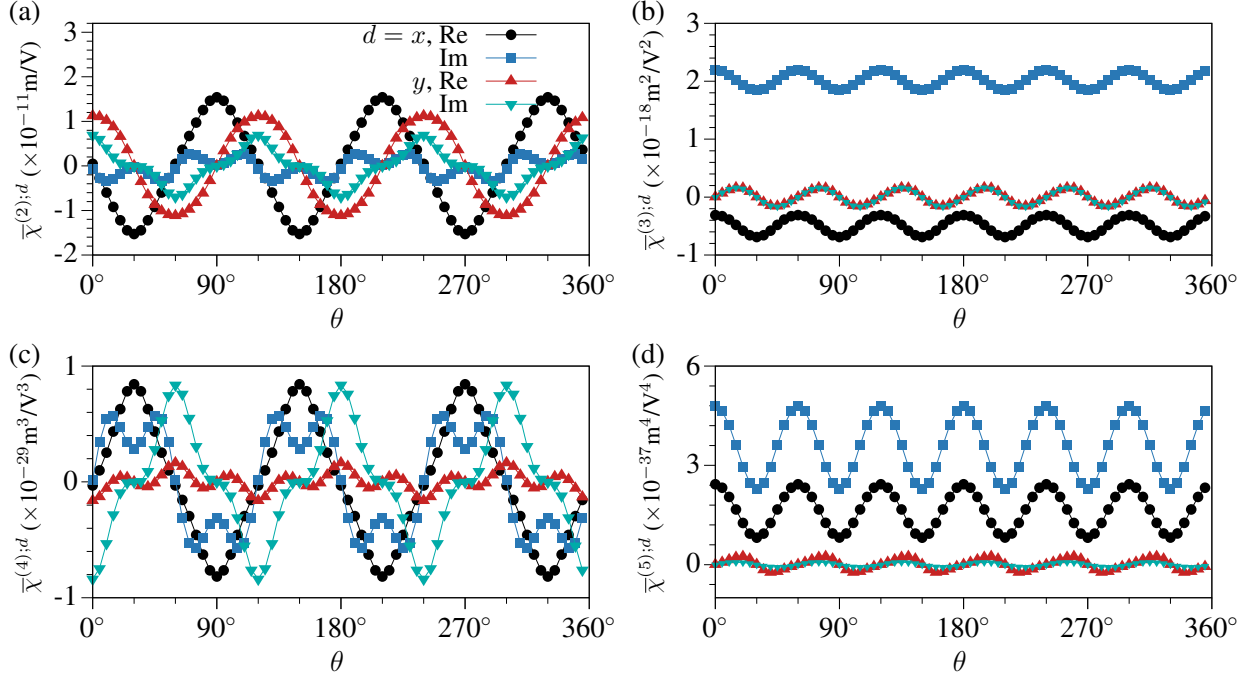


Figure 8: GQD orientation θ dependence of $\bar{\chi}^{(j);d}$ for (a) SHG, (b) THG, (c) FOHG, and (d) FIHG in 4-AC-TQD at an electric field $E_0 = 10^9$ V/m at $\hbar\Omega = 0.91$ eV using the EXE approximation.

Conclusions

We present a comprehensive theoretical investigation of many-body effects on harmonic generations in graphene quantum dots, considering the influences of geometric parameters (shapes, sizes, and edges) and external electric fields. The many-body interactions are modeled through a screened Hartree-Fock approximation and are incorporated into semiconductor Bloch equations. For the ground states, the antiferromagnetic state has the lowest energy, and the Coulomb interaction greatly affects the electronic energy levels and removes the spin degeneracy. For the optical responses, the many-body effects are studied under different approximations: the independent particle approximation, the mean-field approximation, the random phase approximation, and the excitonic effects. The resonant transitions in the mean field approximation have larger transition energies than those in the independent particle approximation, indicating that the energy difference between the LUMO and HOMO levels is enlarged by Coulomb interaction, similar to the GW corrections; for the results obtained

in the random phase approximation, the Hartree term induces local plasmonic resonance to enhance the electric field experienced by the electrons and further blue-shifts the resonant peaks in both linear and nonlinear optical responses; with considering the excitonic effects, the Fock term introduces attractive energy, which red-shifts the transition energies and greatly affects the resonant optical transitions. Interestingly, although the j -photon process leads to a significant resonant peak for the j th-order harmonic generation, the one-photon process leads to negligible resonance in the mean field approximation; however, remarkable resonant peaks appear around the energy for the first linear absorption peak in the random phase approximation and the excitonic effects, indicating a strong influence of the Coulomb interaction on the harmonic generation. We also discussed the impact of the geometric structure of quantum dots, including the size, shape, and edge shapes, on their nonlinear optical properties. Remarkably, the exciton states arising from these nano-structural features exhibit enhanced nonlinear susceptibility compared to that of monolayer graphene. We also studied the electric field dependence. For a very strong electric field, high order harmonics can be generated, but the susceptibility decreases; when the electric field intensity reaches 10^9 V/m, the perturbation theory is no longer applicable. Finally, the polarization pattern dependence is discussed for a single quantum dot and for an ensemble formed by randomly oriented graphene quantum dots. In the latter case, all even-order harmonics vanish, while all odd-order harmonics exist along the polarization direction of the external field, which is similar to an in-plane isotropic system. As a result, our analysis shows that graphene quantum dots exhibit size- and edge-tunable nonlinear optical responses, which establishes a physical basis for possible applications in nonlinear optical devices.

Methods

By denoting the primitive lattice vectors as $\mathbf{a}_1 = (\sqrt{3}/2\hat{x} - 1/2\hat{y})a_0$ and $\mathbf{a}_2 = (\sqrt{3}/2\hat{x} + 1/2\hat{y})a_0$ (see the inset of Fig. 1) with a lattice constant $a_0 = 2.46$ Å, Table 1 lists the methods

to construct these GQDs as well as their information about the numbers of hexagons (N_h) and carbon atoms (N_a). The area S_{QD} is then calculated as $S_{\text{QD}} = N_h \frac{\sqrt{3}}{2} a_0^2$. The position of each carbon atom can be written as $\mathbf{R}_n = n_1 \mathbf{a}_1 + n_2 \mathbf{a}_2 + n_3 (\mathbf{a}_1 + \mathbf{a}_2)/3$ with the abbreviated index $n = (n_1, n_2, n_3)$, where n_1, n_2 are integers and $n_3 = 0$ (1) is for the A (B) site.

Table 1: Numbers of hexagons (N_h) and carbon atoms (N_a) for a N -QD, and methods to construct the centers of all hexagons whose vertexes can generate all locations of carbon atoms in the GQD (construction rules). The construction gives the center positions as $\mathbf{R}_c + l_1 \mathbf{A}_1 + l_2 \mathbf{A}_2$, where \mathbf{R}_c is a position bias that is not important, \mathbf{A}_1 and \mathbf{A}_2 are two vectors, l_1 and l_2 are integers with constraints.

GQD Types	N_h	N_a	\mathbf{A}_i	Constraints
N -AC-TQD	$\frac{3}{2}(N^2 - N) + 1$	$3(N^2 + N)$	$\mathbf{A}_1 = \mathbf{a}_1 + \mathbf{a}_2,$ $\mathbf{A}_2 = 2\mathbf{a}_2 - \mathbf{a}_1$	$0 \leq l_1, l_2, l_1 + l_2 < N$
N -ZZ-TQD	$\frac{1}{2}(N^2 + N)$	$N^2 + 4N + 1$	$\mathbf{A}_i = \mathbf{a}_i$	
N -AC-HQD	$9N^2 - 15N + 7$	$6(3N^2 - 3N + 1)$	$\mathbf{A}_1 = 2\mathbf{a}_1 - \mathbf{a}_2,$ $\mathbf{A}_2 = 2\mathbf{a}_2 - \mathbf{a}_1$	$0 \leq l_1, l_2 < 2N - 1$ $ l_1 - l_2 < N$
N -ZZ-HQD	$3N^2 - 3N + 1$	$6N^2$	$\mathbf{A}_1 = \mathbf{a}_1,$ $\mathbf{A}_2 = \mathbf{a}_2 - \mathbf{a}_1$	

In a simple tight-binding model formed by the $2p_z$ carbon orbitals, the Hamiltonian is

$$\begin{aligned}
\hat{H}(t) = & \sum_{nm,\sigma} h_{nm} \hat{a}_{n\sigma}^\dagger(t) \hat{a}_{m\sigma}(t) \\
& + \frac{1}{2} \sum_{nm,\sigma\sigma'} V_{nm} \hat{a}_{n\sigma}^\dagger(t) \hat{a}_{m\sigma'}^\dagger(t) \hat{a}_{m\sigma'}(t) \hat{a}_{n\sigma}(t) \\
& + |e| \mathbf{E}(t) \cdot \sum_{n,\sigma} \mathbf{R}_n \hat{a}_{n\sigma}^\dagger(t) \hat{a}_{n\sigma}(t),
\end{aligned} \tag{9}$$

where $\hat{a}_{n\sigma}(t)$ ($\hat{a}_{n\sigma}^\dagger(t)$) is the annihilation (creation) operator for the orbital with spin σ located at \mathbf{R}_n , h_{nm} gives the hopping energy between the sites n and m where only the nearest neighbour coupling^{37,42,45,46} is considered with a coupling energy $\gamma_0 = -2.7$ eV, e is the electron charge, and $\mathbf{E}(t)$ is the applied electric field. The second term on the right-hand

side of Eq. (9) gives the electron-electron interaction and V_{nm} is the Ohno potential^{22,47} as

$$V_{nm} = \frac{U}{\epsilon \sqrt{\left(\frac{4\pi\epsilon_0 |\mathbf{R}_n - \mathbf{R}_m| U}{e^2}\right)^2 + 1}}, \quad (10)$$

where $U = 8.29$ eV is the onsite energy and $\epsilon = 3.5$ is used to describe the effective background dielectric constant.

With neglecting the spin-orbit coupling, the electron states can be described by the density matrix

$$\rho_{nm;\sigma}(t) = \langle \hat{a}_{m\sigma}^\dagger(t) \hat{a}_{n\sigma}(t) \rangle, \quad (11)$$

and their dynamics can be described by the semiconductor Bloch equations (SBE) derived from the Green function method at the level of static screened HF approximation

$$i\hbar \frac{\partial \rho_{nm;\sigma}(t)}{\partial t} = [\mathcal{H}_\sigma(t), \rho_\sigma(t)]_{nm} - i\Gamma[\rho_{nm;\sigma}(t) - \rho_{nm;\sigma}^0]. \quad (12)$$

The last term describes the phenomenological relaxation described by the damping parameter Γ , and $\rho_{nm;\sigma}^0$ gives the density matrix at the ground state. The elements of the matrix $\mathcal{H}_\sigma(t)$ are

$$[\mathcal{H}_\sigma(t)]_{nm} = h_{nm} + \delta_{nm} \left[|e| \mathbf{E}(t) \cdot \mathbf{R}_n + \sum_{l,\sigma'} V_{nl} \rho_{ll;\sigma'}(t) \right] - \mathcal{W}_{nm}^0 \rho_{nm;\sigma}(t). \quad (13)$$

Here the term involving V gives the Hartree contribution and the last term gives the Fock contribution³⁷ where $\mathcal{W}_{nm}^0 = W_{nm}^0(0)$ is the static screened Coulomb interaction at equilibrium states. The Hartree term describes the Coulomb potential from the inhomogeneous local charge density, which also induces the local field effects during the optical responses; while the Fock term includes the EXE. The method to determine ρ^0 and \mathcal{W}^0 is given below.

When there is no external electric field, the unperturbed Hamiltonian can be written as

$$\mathcal{H}_{nm;\sigma}^0 = h_{nm} + \delta_{nm} \lambda_{0h} \sum_{l,\sigma'} V_{nl} \rho_{ll,\sigma'}^0 - \lambda_{0f} \mathcal{W}_{nm}^0 \rho_{nm;\sigma}^0, \quad (14a)$$

where λ_{0h} and λ_{0f} are parameters introduced to turn on ($= 1$) or off ($= 0$) the contributions from Hartree and Fock terms at the ground state. The electronic eigenstates are obtained from the Schrödinger equation

$$\sum_m \mathcal{H}_{nm;\sigma}^0 C_{s;m\sigma} = \varepsilon_{s\sigma} C_{s\sigma;n}, \quad (14b)$$

where s is the band index for electronic levels. The density matrix at the ground state is

$$\rho_{nm;\sigma}^0 = \sum_s f_{s\sigma} C_{s\sigma;n} C_{s\sigma;m}^*, \quad (14c)$$

where $f_{s\sigma} = [1 + e^{-(\varepsilon_{s\sigma} - \mu)/(k_B T)}]^{-1}$ is the Fermi-Dirac distribution at a temperature T and chemical potential μ . The chemical potential is related to the total electron number N_e of the GQD through $\sum_{s\sigma} f_{s\sigma} = N_e$. Thus the Green function at the ground state is

$$G_{nm;\sigma}^0(\omega) = \sum_s \left[\frac{1 - f_{s\sigma}}{h\omega - \varepsilon_{s\sigma} + i0^+} + \frac{f_{s\sigma}}{h\omega - \varepsilon_{s\sigma} - i0^+} \right] C_{s\sigma;n} C_{s\sigma;m}^*, \quad (14d)$$

from which the polarization is

$$P_{nm}^0(\omega) = -i\hbar \sum_{\sigma} \int \frac{d\omega_1}{2\pi} G_{nm;\sigma}^0(\omega_1 - \omega) G_{mn;\sigma}^0(\omega_1). \quad (14e)$$

Then the screened Coulomb interaction is written in matrix form as

$$W^0(\omega) = [V^{-1} - P^0(\omega)]^{-1}. \quad (14f)$$

Equations (14a)–(14f) are coupled and they can be solved iteratively. For graphene nanos-

structures with different edges, the ground states can be magnetic.⁴⁸ To consider the possibilities of magnetic ground states, the iteration is performed as follows: starting with a Hamiltonian matrix $\mathcal{H}_{nm;\sigma}^0 = h_{nm} + \delta_{nm}M_{n;\sigma}$ where $M_{n;\sigma}$ is an artificial onsite term depending on the initial magnetic configuration, we iteratively solve Eqs. (14c)–(14f)–(14a)–(14b)–(14d) until achieving the convergence of the density matrix ρ^0 . The ground state is chosen as the lowest energy state among the paramagnetic state using $M_{n;\sigma} = 0$, the ferromagnetic state using $M_{n;\sigma} = \sigma\Delta$, and the antiferromagnetic state using $M_{n;\sigma} = \sigma(2n - 1)\Delta$ with $\Delta = 0.1$ eV.

By applying the electric field $\mathbf{E}(t)$, the dynamics of the density matrix is obtained by solving the SBE in Eq. (12) numerically. To better understand the local field effects and the EXE, we separate the density matrix into two terms

$$\rho(t) = \rho^0 + \rho^e(t). \quad (15)$$

Then the Hamiltonian in Eq. (13) can be rewritten as $\mathcal{H}(t) = \mathcal{H}^0 + \mathcal{H}^e(t)$ with

$$\mathcal{H}_{nm;\sigma}^e(t) = \delta_{nm} \left[\lambda_h \sum_{l,\sigma'} V_{nl} \rho_{ll;\sigma'}^e(t) + |e| \mathbf{E}(t) \cdot \mathbf{R}_n \right] - \lambda_f \mathcal{W}_{nm}^0 \rho_{nm\sigma'}^e(t), \quad (16)$$

where λ_h and λ_f are parameters introduced to turn on ($= 1$) or off ($= 0$) the contributions from Hartree and Fock terms induced by the excited density matrix ρ^e .

In this work, we are interested in the sheet polarization density $\mathbf{P}(t)$ of the system, which is defined as

$$\mathbf{P}(t) = \frac{-|e|}{S_{\text{QD}} d_{\text{gr}}} \sum_n \mathbf{R}_n \sum_{\sigma} \rho_{nn;\sigma}^e(t), \quad (17)$$

with the effective thickness of graphene $d_{\text{gr}} = 3.3 \text{ \AA}$. The definition in Eq. (17) excludes the static polarization, thus the absolute coordinate of the gravity center of the GQD does not affect $\mathbf{P}(t)$. For weak electric fields, the perturbative susceptibilities $\chi^{(i)}$ with different

orders can be defined through

$$\begin{aligned}
P^d(t) = & \int \frac{d\omega}{2\pi} \chi^{(1);da}(\omega) E^a(\omega) e^{-i\omega t} \\
& + \int \frac{d\omega_1 d\omega_2}{(2\pi)^2} \chi^{(2);dab}(\omega_1, \omega_2) E^a(\omega_1) E^b(\omega_2) e^{-i(\omega_1+\omega_2)t} \\
& + \int \frac{d\omega_1 d\omega_2 d\omega_3}{(2\pi)^3} \chi^{(3);dabc}(\omega_1, \omega_2, \omega_3) E^a(\omega_1) E^b(\omega_2) E^c(\omega_3) e^{-i(\omega_1+\omega_2+\omega_3)t} \\
& + \dots,
\end{aligned} \tag{18}$$

where $\mathbf{E}(\omega) = \int dt \mathbf{E}(t) e^{i\omega t}$ gives the Fourier transform of $\mathbf{E}(t)$.

Table 2: Approximations used in this work.

Ground States	λ_{0h}	λ_{0f}	λ_h	λ_f	Response
IPA	0	0	0	0	IPA
MFA	1	1	0	0	MFA
	1	1	1	0	RPA
	1	1	1	1	EXE

Before we present the results, we give a brief summary of the approximations with the four artificially introduced parameters λ_{0h} , λ_{0f} , λ_h , and λ_f . For the ground states, the absence of the electron-electron interaction with $\lambda_{0h} = \lambda_{0f} = 0$ leads to IPA based on the tight-binding model, while its presence with $\lambda_{0h} = \lambda_{0f} = 1$ gives the ground states at HF approximation, which is usually called MFA. For the optical response, $\lambda_h = 1$ includes the feedback of the optical excited charge density distribution, giving the widely discussed RPA;⁴⁹ while a combination of $\lambda_h = 1$ and $\lambda_f = 1$ refers to EXE including the exchange-correlation effects for the optically excited electron-hole pairs, which was not well studied in the literature and is the focus of this work. In Table 2 we list all used approximations.

Acknowledgement

This work has been supported by National Natural Science Foundation of China Grant No. 12034003.

Supporting Information Available

Spectra of nonlinear susceptibilities for different sizes of triangular graphene quantum dots with zigzag edges and hexagonal graphene quantum dots with armchair and zigzag edges (PDF).

References

- (1) Tan, T.; Jiang, X.; Wang, C.; Yao, B.; Zhang, H. 2D Material Optoelectronics for Information Functional Device Applications: Status and Challenges. Adv. Sci. **2020**, 7, 2000058.
- (2) Brida, D.; Tomadin, A.; Manzoni, C.; Kim, Y. J.; Lombardo, A.; Milana, S.; Nair, R. R.; Novoselov, K. S.; Ferrari, A. C.; Cerullo, G.; Polini, M. Ultrafast collinear scattering and carrier multiplication in graphene. Nat. Commun. **2013**, 4, 1987.
- (3) Tokman, M.; Bodrov, S. B.; Sergeev, Y. A.; Korytin, A. I.; Oladyshkin, I.; Wang, Y.; Belyanin, A.; Stepanov, A. N. Second harmonic generation in graphene dressed by a strong terahertz field. Phys. Rev. B **2019**, 99, 155411.
- (4) Oum, K.; Lenzer, T.; Scholz, M.; Jung, D. Y.; Sul, O.; Cho, B. J.; Lange, J.; Müller, A. Observation of Ultrafast Carrier Dynamics and Phonon Relaxation of Graphene from the Deep-Ultraviolet to the Visible Region. J. Phys. Chem. C **2014**, 118, 6454–6461.
- (5) Autere, A.; Jussila, H.; Dai, Y.; Wang, Y.; Lipsanen, H.; Sun, Z. Nonlinear Optics with 2D Layered Materials. Adv. Mater. **2018**, 30, e1705963.
- (6) Jiang, T. et al. Gate-tunable third-order nonlinear optical response of massless Dirac fermions in graphene. Nat. Photon. **2018**, 12, 430–436.
- (7) Mikhailov, S. A. Non-linear electromagnetic response of graphene. EPL **2007**, 79, 27002.

- (8) Mikhailov, S. A.; Ziegler, K. Nonlinear electromagnetic response of graphene: frequency multiplication and the self-consistent-field effects. J. Phys.: Condens. Matter **2008**, 20, 384204.
- (9) Zhou, R.; Guo, T.; Huang, L.; Ullah, K. Engineering the harmonic generation in graphene. Mater. Today Phys. **2022**, 23, 100649.
- (10) Bonaccorso, F.; Sun, Z.; Hasan, T.; Ferrari, A. C. Graphene photonics and optoelectronics. Nat. Photon. **2010**, 4, 611–622.
- (11) Wang, F.; Zhang, Y.; Tian, C.; Girit, C.; Zettl, A.; Crommie, M.; Shen, Y. R. Gate-Variable Optical Transitions in Graphene. Science **2008**, 320, 206–209.
- (12) Tomadin, A.; Horneett, S. M.; Wang, H. I.; Alexeev, E. M.; Candini, A.; Coletti, C.; Turchinovich, D.; Kläui, M.; Bonn, M.; Koppens, F. H. L.; Hendry, E.; Polini, M.; Tielrooij, K.-J. The ultrafast dynamics and conductivity of photoexcited graphene at different Fermi energies. Sci. Adv. **2018**, 4, eaar5313.
- (13) Yavari, F.; Kritzinger, C.; Gaire, C.; Song, L.; Gulapalli, H.; Borca-Tasciuc, T.; Ajayan, P. M.; Koratkar, N. Tunable Bandgap in Graphene by the Controlled Adsorption of Water Molecules. Small **2010**, 6, 2535–2538.
- (14) Cai, J.; Pignedoli, C. A.; Talirz, L.; Ruffieux, P.; Söde, H.; Liang, L.; Meunier, V.; Berger, R.; Li, R.; Feng, X.; Müllen, K.; Fasel, R. Graphene nanoribbon heterojunctions. Nat. Nanotechnol. **2014**, 9, 896–900.
- (15) Datta, S. S.; Strachan, D. R.; Khamis, S. M.; Johnson, A. T. C. Crystallographic Etching of Few-Layer Graphene. Nano Lett. **2008**, 8, 1912–1915.
- (16) Campos, L. C.; Manfrinato, V. R.; Sanchez-Yamagishi, J. D.; Kong, J.; Jarillo-Herrero, P. Anisotropic Etching and Nanoribbon Formation in Single-Layer Graphene. Nano Lett. **2009**, 9, 2600–2604.

- (17) Li, M.; Li, L.; Fan, Y.; Jiao, F.; Geng, D.; Hu, W. From Top to Down-Recent Advances in Etching of 2D Materials. Adv. Mater. Interfaces **2022**, 2201334.
- (18) Güçlü, A. D.; Potasz, P.; Hawrylak, P. Excitonic absorption in gate-controlled graphene quantum dots. Phys. Rev. B **2010**, 82, 155445.
- (19) Castro Neto, A. H.; Guinea, F.; Peres, N. M. R.; Novoselov, K. S.; Geim, A. K. The electronic properties of graphene. Rev. Mod. Phys. **2009**, 81, 109–162.
- (20) Dutta, S.; Pati, S. K. Novel properties of graphene nanoribbons: a review. J. Mater. Chem. **2010**, 20, 8207–8223.
- (21) Wei, J.; Xu, Q.; Xu, Z.; Wang, W.; Meng, S.; Bai, X. Dynamic Observation of the Coulomb Explosion and Field Evaporation of a Few-Layer Graphene Nanoribbon. Small **2023**, 19, 2300226.
- (22) Sadeq, Z. S.; Muniz, R. A.; Sipe, J. E. Role of impurities on the optical properties of rectangular graphene flakes. Phys. Rev. Materials **2018**, 2, 014001.
- (23) Aguillon, F.; Borisov, A. G. Atomic-Scale Defects Might Determine the Second Harmonic Generation from Plasmonic Graphene Nanostructures. J. Phys. Chem. Lett. **2023**, 14, 238–244.
- (24) Sk, M. A.; Ananthanarayanan, A.; Huang, L.; Lim, K. H.; Chen, P. Revealing the tunable photoluminescence properties of graphene quantum dots. J. Mater. Chem. C **2014**, 2, 6954–6960.
- (25) Tiutiunnyk, A.; Laroze, D.; Correa, J.; Mora-Ramos, M. Electronic and magnetic properties of stacked graphene quantum dots. Diam. Relat. Mater. **2023**, 131, 109550.
- (26) Buzaglo, M.; Shtein, M.; Regev, O. Graphene Quantum Dots Produced by Microfluidization. Chem. Mater. **2016**, 28, 21–24.

- (27) Nesakumar, N.; Srinivasan, S.; Alwarappan, S. Graphene quantum dots: synthesis, properties, and applications to the development of optical and electrochemical sensors for chemical sensing. Microchim. Acta **2022**, 189, 258.
- (28) Kalluri, A.; Dharmadhikari, B.; Debnath, D.; Patra, P.; Kumar, C. V. Advances in Structural Modifications and Properties of Graphene Quantum Dots for Biomedical Applications. ACS Omega **2023**, 8, 21358–21376.
- (29) Cox, J. D.; Javier García de Abajo, F. Electrically tunable nonlinear plasmonics in graphene nanoislands. Nat. Commun. **2014**, 5, 5725.
- (30) Cox, J. D.; Marini, A.; de Abajo, F. J. G. Plasmon-assisted high-harmonic generation in graphene. Nat. Commun. **2017**, 8, 14380.
- (31) Avchyan, B. R.; Ghazaryan, A. G.; Sargsyan, K. A.; Sedrakian, K. V. On Laser-Induced High-Order Wave Mixing and Harmonic Generation in a Graphene Quantum Dot. JETP Letters **2022**, 116, 428–435.
- (32) Gnawali, S.; Ghimire, R.; Magar, K. R.; Hossaini, S. J.; Apalkov, V. Ultrafast electron dynamics of graphene quantum dots: High harmonic generation. Phys. Rev. B **2022**, 106, 075149.
- (33) Gnawali, S.; Apalkov, V. High harmonic generation governed by edge states in triangular graphene quantum dots. Phys. Rev. B **2023**, 108, 115434.
- (34) Yang, L. Excitonic Effects on Optical Absorption Spectra of Doped Graphene. Nano Lett. **2011**, 11, 3844–3847.
- (35) Mueller, T.; Malic, E. Exciton physics and device application of two-dimensional transition metal dichalcogenide semiconductors. npj 2D Mater. Appl. **2018**, 2, 29.
- (36) Song, Y.; Shan, Y.; Wang, W.; Chang, K.; Zheng, Z.; Shi, Z.; Li, D.; Cheng, J. L.

- Second Harmonic Generation in Exfoliated Few-Layer ReS₂. Adv. Opt. Mater. **2023**, 11, 2300111.
- (37) Cheng, J. L.; Sipe, J. E.; Guo, C. Third harmonic generation of undoped graphene in Hartree-Fock approximation. Phys. Rev. B **2019**, 100, 245433.
- (38) Yang, L.; Deslippe, J.; Park, C.-H.; Cohen, M. L.; Louie, S. G. Excitonic Effects on the Optical Response of Graphene and Bilayer Graphene. Phys. Rev. Lett. **2009**, 103, 186802.
- (39) Hwang, E. H.; Hu, B. Y.-K.; Das Sarma, S. Density Dependent Exchange Contribution to $\partial\mu/\partial n$ and Compressibility in Graphene. Phys. Rev. Lett. **2007**, 99, 226801.
- (40) Cheng, J. L.; Vermeulen, N.; Sipe, J. E. Numerical study of the optical nonlinearity of doped and gapped graphene: From weak to strong field excitation. Phys. Rev. B **2015**, 92, 235307.
- (41) Boyd, R. W. Nonlinear Optics, 3rd ed; Academic, New York, 2008.
- (42) Cheng, J. L.; Vermeulen, N.; Sipe, J. E. Third order optical nonlinearity of graphene. New J. Phys. **2014**, 16, 053014.
- (43) Hong, S.-Y.; Dadap, J. I.; Petrone, N.; Yeh, P.-C.; Hone, J.; Osgood, R. M. Optical Third-Harmonic Generation in Graphene. Phys. Rev. X **2013**, 3, 021014.
- (44) Kumar, N.; Kumar, J.; Gerstenkorn, C.; Wang, R.; Chiu, H.-Y.; Smirl, A. L.; Zhao, H. Third harmonic generation in graphene and few-layer graphite films. Phys. Rev. B **2013**, 87, 121406.
- (45) Cheng, J. L.; Vermeulen, N.; Sipe, J. E. Third-order nonlinearity of graphene: Effects of phenomenological relaxation and finite temperature. Phys. Rev. B **2015**, 91, 235320.
- (46) Cheng, J. L.; Vermeulen, N.; Sipe, J. E. DC current induced second order optical nonlinearity in graphene. Opt. Express **2014**, 22, 15868–15876.

- (47) Jiang, J.; Saito, R.; Samsonidze, G. G.; Jorio, A.; Chou, S. G.; Dresselhaus, G.; Dresselhaus, M. S. Chirality dependence of exciton effects in single-wall carbon nanotubes: Tight-binding model. Phys. Rev. B **2007**, 75, 035407.
- (48) Yazyev, O. V. Emergence of magnetism in graphene materials and nanostructures. Rep. Prog. Phys. **2010**, 73, 056501.
- (49) Cox, J. D.; García de Abajo, F. J. Plasmon-Enhanced Nonlinear Wave Mixing in Nanostructured Graphene. ACS Photonics **2015**, 2, 306–312.

TOC Graphic

